Int J Adv Manuf Technol (2016) 82:631–643
DOI 10.1007/s00170-015-7390-x

ORIGINAL ARTICLE

Interface microstructure and fracture behavior of single/dual-beam laser welded steel-Al dissimilar joint produced with copper interlayer

Shuhai Chen[1] · **Zhiliang Zhai**[1] · **Jihua Huang**[1] · **Xingke Zhao**[1] · **Jiguang Xiong**[1]

Received: 17 February 2015 / Accepted: 3 June 2015 / Published online: 17 June 2015

Abstract Dissimilar metal welding of Q235 low carbon steel and 5052 aluminum alloy was carried out by a single/dual-beam laser in a steel-on-aluminum overlap configuration with a copper interlayer. The weld appearance, microstructure, and fracture behavior of the joints made by the single/dual-beam laser welding were investigated comparatively. The results showed that dual-beam laser welding, compared with single-beam laser welding, had better process stability which made better weld appearance and bigger effective joining width which enhanced tensile capacity. With a copper interlayer, a contact reaction zone appeared between the copper interlayer and aluminum matrix, which enlarged effective joining zone. The microstructures of the welding joint welded by a single/dual-beam laser were composed of the ligulate fusion zone with Fe-Al interface and the contact reaction brazing zone with Al-Cu interface. The Fe-Al interface mainly consisted of α-Al and Al_2Cu eutectic structure, FeAl, $FeAl_2$, and a certain amount of Al-Cu intermetallics, Fe_2Al_5 and $FeAl_3$. The Al-Cu interface mainly consisted of eutectic phase Al_2Cu and metastable phase of Al-Cu intermetallics. The tensile property was enhanced by a dual-beam laser, and the addition of the copper-foil interlayer might improve the metallurgical reaction of interfacial reaction region and promote the load-carrying ability of weld joint. An ideal joint with fewer defects could be obtained when the welding speed is 0.9–1.25 m/min of dual-beam laser welding and 1.5–1.75 m/min of single-beam laser welding.

✉ Jihua Huang
jihuahuang47@sina.com

[1] School of Materials Science and Engineering, University of Science and Technology Beijing, Beijing 100083, People's Republic of China

Keywords Steel/aluminum dissimilar metals · Single/dual-beam laser · Copper interlayer · Contact reaction brazing zone

1 Introduction

In recent years, lightweight automobiles have attracted more attention than ever because of increasingly serious problems of energy source crisis and vehicle exhaust pollution [1–5]. For the purpose of mass reduction, aluminum industry was developed. But it has been costly to manufacture automobiles mainly with aluminum parts [6]. Therefore, the use of composite structure made of steel/aluminum dissimilar alloys is an effective and popular solution to save on mass and keep expenses reasonably low [7]. However, the formation of a mass of intermetallic compounds (IMCs), such as $FeAl_3$, Fe_2Al_5, and $FeAl_2$, badly deteriorates mechanical properties of the composite joint because IMCs are known to be brittle [1, 4, 8]. Increasing the composite structures of aluminum and steel in the auto body would require technological advancements in the dissimilar joining process of these two alloys [6]. To eliminate or improve Fe-Al IMCs and achieve a reliable welding of these two alloys, various researches have been conducted on this topic. Some of novel welding methods, such as laser/arc welding-brazing [9–13], resistance/laser spot welding [14–16], friction stir/friction welding [17–20], and explosion welding [21, 22], were explored to suppress the formation of the Fe-Al IMCs, and these new welding methods can also to be used in Al alloys, steels, and dissimilar joining of these two materials [23–25].

One of the main processes used for joining aluminum to steel has been laser welding. Laser welding has high welding speed which can limit metallurgical reaction time to very short levels. Hence, the formation of IMCs can be suppressed

effectively [7]. Some researchers have investigated this method and optimized the joint property, but it is restricted to process parameters [1] and heat source mode including laser keyhole welding [4] and heat conduction welding [26]. In fact, difficulty of dissimilar material joining could be attributed to the problem of welding metallurgy. Improving IMCs' morphological distribution and forming a new intermetallic compound with better mechanical property are two important ways to enhance the mechanical property of the Fe-Al joint. These could be achieved by the means of metallurgical methods. In our previous investigations [7], a Ni interlayer placed between steel and aluminum could improve the liquid Fe-Al reaction and enhance toughness of Fe-Al composite joint from the view of improving metallurgical reaction. Similarly, in the present study, a copper interlayer was placed between steel and aluminum to suppress the formation of IMCs from the view of improving metallurgical reaction of the weld molten pool.

Moreover, under a single-beam laser, the effective joining width is narrow at the contact flat plane of the composite lap joint, where the steel penetrates in the aluminum. As a result, the load capacity of the joint welded by a single-beam laser is limited in use. Increasing the effective joining width may improve the carrying capacity. Dual-beam laser welding could control the formation of IMCs and increase the effective joining width and then the joint property may be enhanced. Yan et al. used a dual-beam YAG laser to weld dissimilar steel and aluminum alloys in a lap-joint configuration [5]. They reported that a dual-beam laser could control IMC layer width and enhanced shearing strength. Miyashita et al. performed dual-beam laser welding of magnesium to aluminum [27]. They declared that the application of dual-beam technique could control temperature distribution and flow behavior of the molten metal combined with reasonable beam distance. As a result, it changed the formation of IMCs at the interface of the joint and resulted in an increase in the failure load of the joints. Harooni et al. used a fiber laser to weld magnesium alloy by a single/dual-beam laser in a zero-gap lap-joint configuration [3]. It was found that the shear strength of the dual-beam laser-welded samples was higher than that in case of single-beam laser-welded samples. Chen et al. used a dual-beam laser with zero inter-beam distance to weld aluminum alloys in lap-joint configuration [28]. They revealed that the weld bead obtained from dual-beam laser welding produced higher strength than that obtained from single-beam laser welding. Therefore, dual-beam laser welding was also proposed in the laser welding of metals in the present study.

In the present study, a steel-on-aluminum overlap configuration between the Q235 steel 5052 Al alloy was welded by a single/dual-beam laser in keyhole welding mode with a copper-foil interlayer. By means of the single/dual-beam comparisons, the influences of welding speed or linear energy on weld appearances, joint microstructures, and fracture behaviors were discussed. In dissimilar material welding, the metallurgical behavior is a key factor to improve the joining strength. Thus, not only the steel/aluminum interface but also the aluminum/copper interface was analyzed to investigate joining mechanisms in the interfacial reaction layers.

2 Materials and experimental procedures

2.1 Materials

Dissimilar materials chosen for investigation were Q235 low carbon steel mostly used for automotive applications and 5052 Al alloy with a wide range of applications in aeronautical and high-speed vehicle fields. Their dimensions are all 100×70×1 mm^3, and their nominal chemical compositions are listed in Table 1. A copper-foil interlayer with a dimension of 110×5×0.1 mm^3 was placed in the steel-on-aluminum overlap configuration. Physical properties of the materials are shown in Table 2. Before welding process, the surfaces of the sheets were polished by grade 1200 SiC paper to remove oxide film and then degreased with acetone. During welding operation, both of the overlapped coupons were tightly clamped to ensure a zero gap.

2.2 Single/Dual-beam laser welding procedure

A high-power axial-flow CO_2 laser system with a maximum output power of 4 kW was employed in TEM_{01} mode. In the laser equipment, a parabolic reflector has a fixed focal length of 200 mm, and the focus point with a diameter of 0.2 mm was

Table 1 Chemical composition of the alloys used in this study, wt% [20, 21]

Materials	Element											
	Al	Fe	Cr	Mn	Mg	Cu	Si	Ti	Zn	S	P	C
5052	Bal.	≤0.4	0.15–0.35	≤0.1	2.2–2.8	≤0.1	≤0.25	2.2–2.8	≤0.1	–	–	–
Q235	–	Bal.	–	0.3–0.65	–	–	≤0.3	–	–	≤0.05	≤0.045	0.14–0.22

"–" means the element does not exist in the alloy

Table 2 Physical properties of materials used in this study [20]

Materials	5052	Q235	Cu
Melting point (°C)	649	1350	1083
Thermal expansion coefficient (10^{-6}/K)	23.8	12.6	17.6
Thermal conductivity (W/m K)	138	60	386
Specific heat capacity (J/g °C)	0.88	0.46	0.39
Relative density (g/cm^3)	2.68	7.85	8.93

on the upper surface of the steel in the steel-on-aluminum overlap configuration. An argon shielding gas nozzle with a flow rate of 15 L/min was set to protect heated surfaces from oxidation.

The single beam was split into dual beams by a wedge reflector copper mirror before laser beam was focused by the parabolic reflector copper mirror, as shown in Fig. 1a. The distance of the dual-beam laser focus points is as small as 0.8 mm. During dual-beam laser welding, the line of the both focus points is vertical with welding direction.

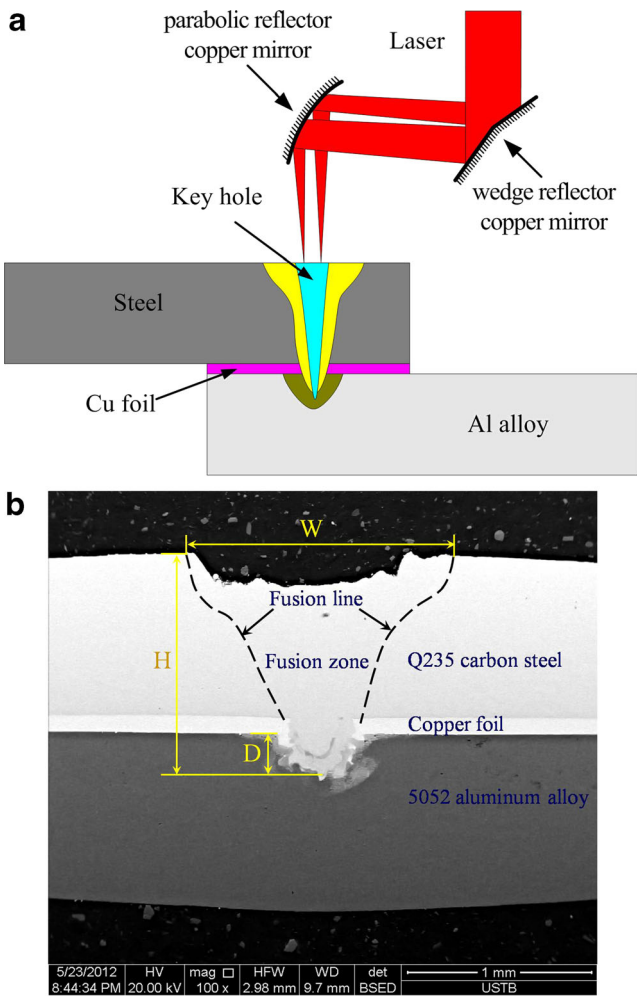

Fig. 1 Schematic illustration of **a** dual-laser beam welding system and **b** the weld appearance parameters

Laser power and welding speed were chosen at the range of 1–3 kW and 0.5–3.0 m/min, respectively. According to the preliminary experimental trials, the optimum single-beam laser power was 1.6 kW, and that of the dual-beam laser corresponded to 2.5 kW. By varying the welding speed, the specimens were obtained under different heat inputs. The main parameters used in the present study are listed in Table 3.

2.3 Metallurgical and mechanical characterizations

Cross sections of the specimens, which were all etched by solutions with a volume fraction of 2 % HF, 10 % HNO_3, and 88 % H_2O for about 10 s, were prepared for microstructure observation in the metallographic method. Tensile strength of the joints was evaluated at room temperature by an electronic tension machine at a cross-head speed of 1 mm/min. Transverse cross sections and fracture surfaces were analyzed by means of scanning electron microscope (SEM) equipped with an energy-dispersive X-ray spectroscopy (EDS) detector (working voltage 200–300 V, resolution 3.5 nm) for chemical constitution analysis. The hardness at the joints was measured using a Vickers microhardness tester with a load of 10 g and a dwell time of 10 s.

2.4 Evaluation parameters of weld bead

The following weld appearance parameters were determined for each sample using image analysis technique: weld width (W), weld penetration depth (H), and penetration depth of steel plunging into aluminum alloy (D). The schematic illustration of the weld appearance parameters is shown in Fig. 1b.

Table 3 Laser welding parameters used in the present experiment

Test No.	Beam type	Laser power (kW)	Welding speed (m/min)	Linear energy (J/mm)
1	Single	1.6	1	96
2			1.25	76.8
3			1.5	64
4			1.75	54.86
5			2	48
6			2.25	42.67
7	Dual	2.5	0.75	200
8			0.85	176.47
9			0.9	166.67
10			0.95	157.89
11			1	150
12			1.25	120
13			1.5	100
14			2.25	66.67

In this paper, the heat input was expressed by liner energy Q, which is welding bead heat input per unit length. It was calculated by

$$Q = 60P \Big/ 1000V \quad (1)$$

where P is the laser power and V is the welding speed.

The joint zone of the tensile specimens for the overlap configuration rotated during mechanical test because two forces in the specimen were not in line. Consequentially, a torque was generated. We do not evaluate whether the forces are shear or tensile. The normalized stress at failure (based on bonded area or fracture area) was not calculated. The tensile property was expressed as the maximal load per millimeter, i.e., linear failure strength (N/mm). The average value of three samples as a data point of tensile property was used at the same parameter.

3 Experimental results and discussion

3.1 Weld appearance of single/dual beam

3.1.1 Characteristic of the weld surface

Figure 2 shows the macroscopic photograph of typical upper weld beads. Figure 2a, b shows weld beads that were welded by a single-beam laser (1.6 kW) under the parameters of NO. 2 (Q=76.8 J/mm, W=1.14 mm) and NO. 3 (Q=64 J/mm, W=1.01 mm), respectively. Figure 2c shows a weld bead that was welded by a dual-beam laser (2.5 kW) under the parameters of NO. 14 (Q=66.67 J/mm, W=1.46 mm). The weld width of weld bead welded by the dual-beam laser is wider than that welded by single-beam laser even though a larger linear energy (NO. 2) is used for the single-beam welding. One of the tremendous causes is that the distance between the two beams' focused points is 0.8 mm. It indicates that the dual-beam laser itself has the advantage of increasing the weld width.

As shown in Fig. 2a, b, weld defects, such as welding spatters, formation discontinuities, and surface pores, can be observed in the weld bead welded by a single-beam laser. However, the top surface quality of the weld bead obtained with dual-beam laser welding is smoother and more uniform than that obtained with single-beam laser welding, which could benefit from better welding process stability of dual beam than single beam.

3.1.2 Characteristic of the weld cross section

Figure 3 shows cross sections of the overlapped joints by a single/dual-beam laser. Figure 3a–f shows cross sections that were obtained by single-beam laser under the parameters from NO. 1 to 6, and Fig. 3g–m shows cross sections that were acquired by dual-beam laser under the parameters from NO. 7 to 13. The statistic weld appearance parameters under different welding speeds of single/dual-beam laser are shown in Fig. 4. As shown in Fig. 4, all the parameters, W, H, and D, roughly decrease as the welding speed increases under both single- and dual-beam laser. When welding speed was smaller or larger than a certain value, composite joints exhibited an unstable weld appearance characteristic under single/dual-beam laser. The weld appearance characteristic was exhibited stable only when the welding speed was controlled within a neutral range. The relatively suitable range of welding speed was 0.85–1.25 m/min of dual-beam laser and 1.25–2.0 m/min of single-beam laser, respectively. At the suitable range, the W of dual beam was larger than that of single beam, the D of dual beam was smaller than that of single beam, and the H of single beam was similar than that of dual beam.

Under the same laser power of single/dual-beam laser, varying welding speed will cause different degrees of weld defects, such as concavities, gaps, and cracks. As shown in Fig. 3a, g, the top margin of steel seam is seriously concave

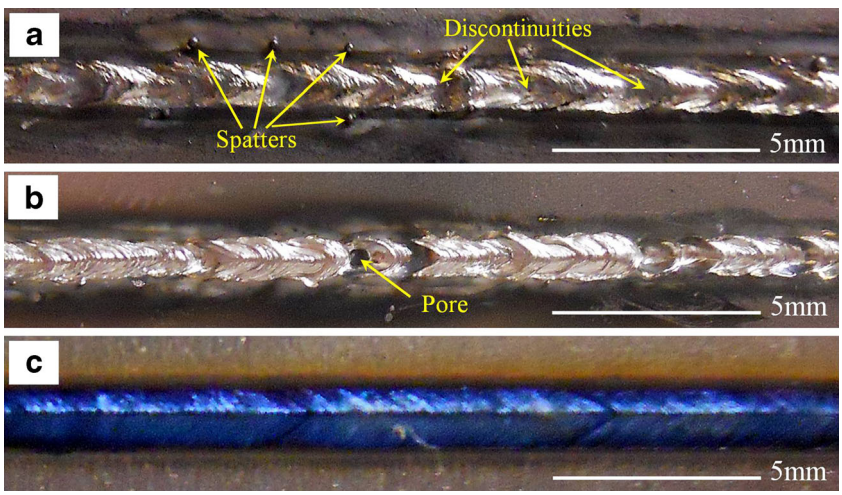

Fig. 2 Upper weld beads of Q235/5052 lap joints with copper interlayer: **a**, **b** beads welded by single-beam laser under the parameters of NO. 2 and 3, respectively; **c** beads welded by dual-beam laser under the parameters of NO. 14

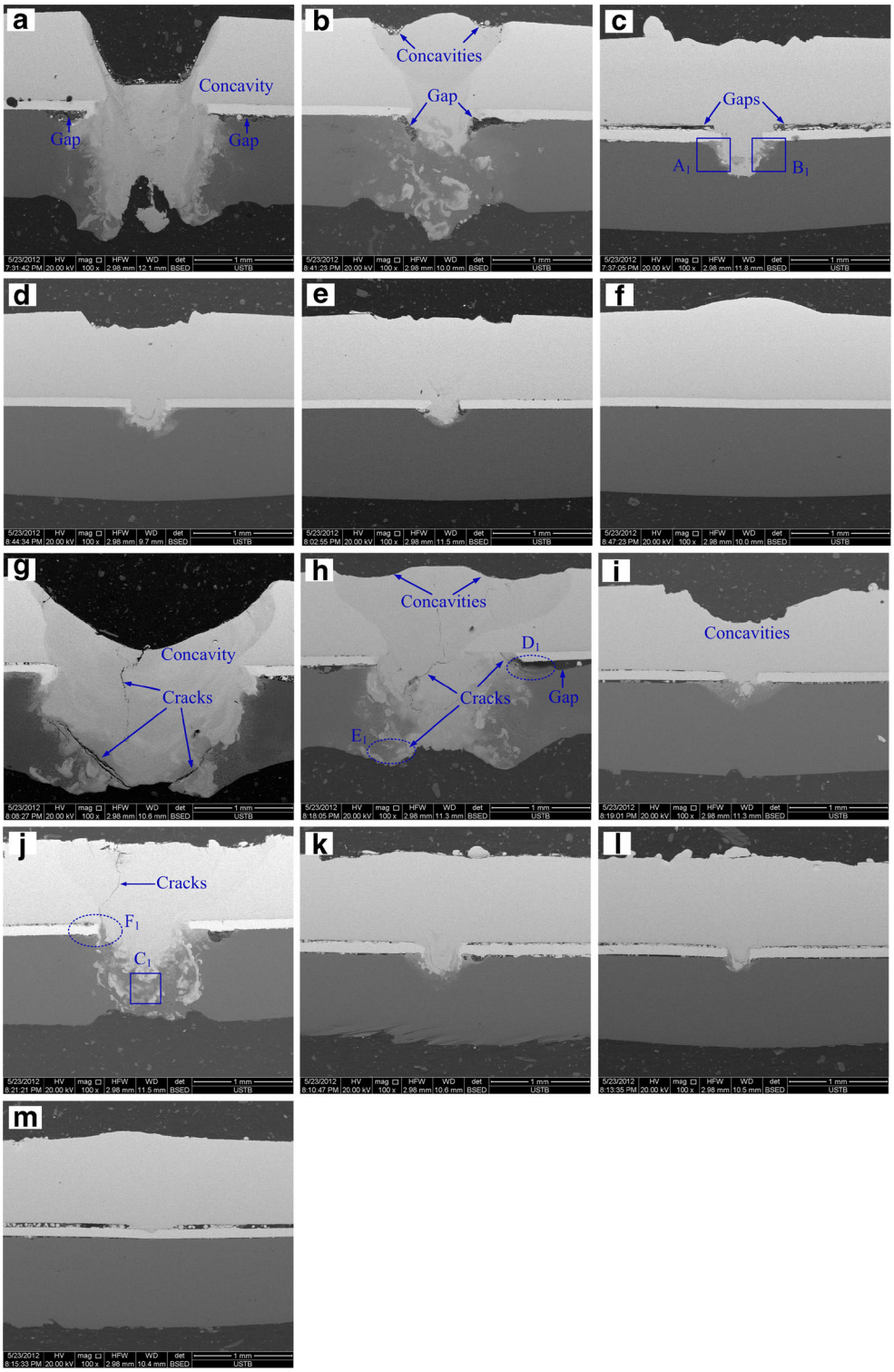

Fig. 3 Cross section shapes of the welds **a**–**f** obtained by single-beam laser under the parameters from NO. 1 to 6 and **g**–**m** acquired by dual-beam laser under the parameters from NO. 7 to 13

downward for relatively low welding speed. Two concavities could be observed clearly in Fig. 3b, h. The top margin of steel seam becomes more uniform in Fig. 3c–e, j–l. However, the effective joining even cannot be achieved in Fig. 3f, m for relatively high welding speed. Therefore, from the view of the joint performance, an ideal joint with fewer defects could be obtained by a suitable welding speed under the same laser power of single/dual-beam laser. Combined with the abovementioned optimization range of welding speed, a re-optimization range of welding speed is 0.9–1.25 m/min of dual-beam laser and 1.5–1.75 m/min of single-beam laser.

A dual-beam laser welding joint with relatively high heat input tends to generate more cracks. Crack propagation happened at the fusion steel/Al interface and seam centerline, as

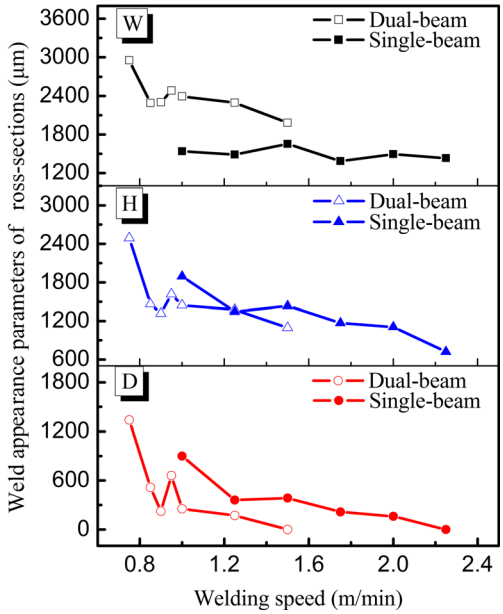

Fig. 4 Weld appearance parameters under different welding speeds of single/dual beam

shown in Fig. 3g, h, j. Two possible reasons to interpret the phenomenon are the following. On the one hand, due to the extremely high cooling rate during the welding, around hundreds of degrees per second, solid solution in the molten pool was mainly martensite phase. Martensite is usually brittler than the Al alloy and has poor deforming capacity. As a result, hot cracking took place when the alloy was semisolid during the final stage of solidification [29, 30]. On the other hand, the weakest joining location, such as the serious swell at the bottom of the joint (the oval region E_1 in Fig. 3h) and the small copper convex formed near the molten pool (the oval region D_1 in Fig. 3h, and F_1 in Fig. 3g), produced quite large stress concentration, which induced the generation of cracks under thermal stress due to the mismatch of the thermal expansion [30].

3.2 Microstructures of the overlapped steel-on-aluminum joints with copper interlayer

The welding joint is composed of two regions with different morphological features. One is the ligulate fusion zone embedding aluminum matrix, and the other is the weld extension region between copper interlayer and aluminum matrix at the upper margins of ligulate fusion zone, which is considered to be formed by contact reaction brazing. The two features will be discussed, respectively.

3.2.1 Ligulate fusion zone

In the cross section of every effective joint welded by single/dual-beam laser, a ligulate fusion zone is indispensable to join the Fe-Al dissimilar alloys. A clear Fe-Al interfacial reaction layer of the ligulate fusion zone is shown in Fig. 5a, which is magnification of zone A_1 in Fig. 3c. The IMCs in the interfacial layer were composed of two layers with different characteristics. One was the gray zone along the dotted line, and the other was the network structure close to the side of Al alloy, which spread along the border of the fusion zone. The thickness of the network structure at the top is wider than that at the bottom. Figure 5b shows magnification of the network region (plotted by a rectangular mark M_2 in Fig. 5a). From Al alloy to the fusion zone, a slender ribbon-shaped or distinct dendrite structure inlayed into aluminum alloy, a network structure, and a comparatively wide ribbon-shaped structure could be observed clearly. Perhaps the reason was that the Cu atoms at the both sides of the fusion zone was mixed into the Al alloy and transformed into IMCs with the temperature decreasing.

The EDS test was performed to identify IMC phase compositions. In terms of Fe-Cu binary phase diagram, there are no intermetallic phases and only Fe-rich bcc solid solution or Cu-rich fcc solid solution exists [31–33]. As a result, IMCs in the present study were considered to be only involved in Fe-Al and Al-Cu binary system. According to the reports in the literatures [1, 6, 12, 26, 34, 35], the Fe-Al IMC phases were determined by the atomic percent of the iron and aluminum (listed in Table 4). Similarly, different Al-Cu IMC phases with different atomic percent of the aluminum and copper (listed in Table 5) were obtained from the references [32, 36–38].

The EDS results at the zones A_2 to D_2 in Fig. 5a are shown in Table 6. The element compositions at the zones A_2 and D_2 are close to the parents of steel and Al alloy, respectively. Thus, phase compositions were considered to be no change in the ligulate fusion zone and Al alloy, respectively. At the B_2 zone, the Al content is higher than the total amount of Fe and Cu. According to the typical laser welding of steel-aluminum reported by Ma J et al. [6], the gray zone in the interfacial layer was identified as FeAl and $FeAl_2$. Besides, the Cu content was high enough to generate Al-Cu intermetallics, according to the Al-Cu binary phase diagram [37]. Therefore, the gray zone (zone B_2) might consist of FeAl and $FeAl_2$, even a certain amount of Al-Cu intermetallics. Based on the Al-Cu binary phase diagram [37] and the reported literature [38] about the intermediate layer of laser welding copper-aluminum, the network structure (zone C_2) was near-eutectic structure and it was mainly composed of α-Al phase and Al-rich phase Al_2Cu.

The line scanning results in Fig. 5c shows the distribution of Fe, Cu, and Al elements at the Fe-Al interface layer. As shown in Fig. 5c, the Al-Cu reaction layer and the Fe-Cu-Al reaction layer were approximately 30 and 60 μm in thickness, respectively. Compared with zones A_2–D_2 in Fig. 5a, the Al-Cu reaction layer are equivalent to the network structure (zone C_2), and the Fe-Cu-Al reaction layer corresponds to the gray zone (zone B_2). At the Al-Cu reaction layer, the IMC Al_2Cu in the network structure was confirmed due to the relatively high content of Al and Cu, according to the Al-Cu binary phase diagram [37]. At the Fe-Cu-Al reaction layer, the Fe content

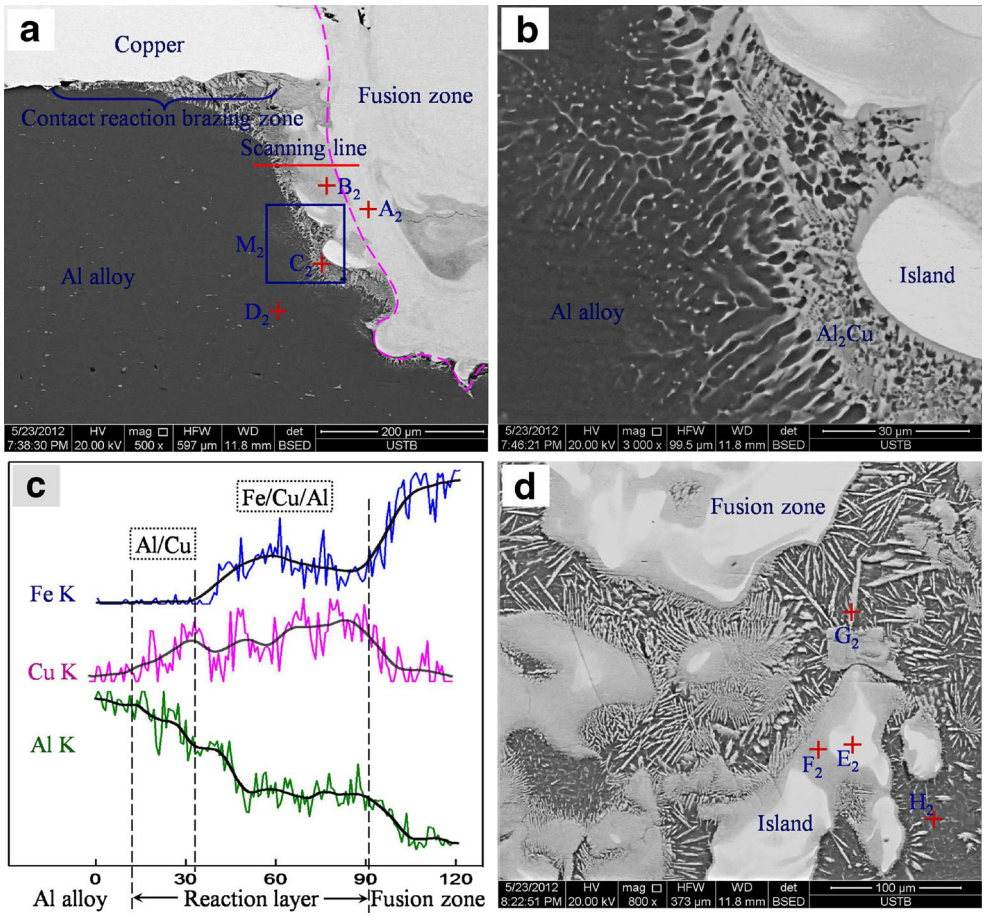

Fig. 5 Microstructures of the ligulate fusion zone mainly from different locations in Fig. 3: **a** from position A_1 of Fig. 3c under a single-beam laser, **b** area M_2 in (**a**), **c** results of line scanning in (**a**), and **d** from area C_1 in Fig. 3j under a dual-beam laser

increased to a certain value and then remained stable. The Al content decreased to a certain value and then remained basically stable. The common relatively stable section of Fe and Al content indicated that some intermetallic compounds between Fe and Al were formed in the interlayer. Because the Cu content in the interlayer was relatively high, a certain amount of Al-Cu intermetallics might be formed, according to the Al-Cu binary phase diagram [37].

However, when the welding speed of single/dual beam was smaller than 1.25/0.95 m/min, large amounts of isolated steel islands appeared. As shown in Fig. 3a, b (single beam) and g–j (dual beam), the steel penetrating in Al alloy formed isolated steel islands distributed in the bottom of the ligulate fusion zone. Compared with single-beam laser, the amount of steel islands obtained by a dual-beam laser was more, and its distribution was much more complicated. Besides, with regard to single/dual-beam laser, the amount of steel islands was larger and its distribution was much more disordered when using a lower welding speed. Figure 5d shows the magnification of zone C_1 in Fig. 3j. As shown in Fig. 5d, the light island phases dissociated in the Al alloy near the fusion zone. Between the island phases and the fusion zone, large amounts of needle-sharp phases with an average dimension of approximately 50×5 μm grew scattering around the isolated steel islands or the fusion zone.

During laser keyhole welding, the fusion zone was firstly formed with unstable joining interfaces under the laser beam. With the increasing of linear energy or the decreasing of welding speed, the joining interface fluctuated more intensely. Once the welding speed was out of the certain value, large amounts of steel escaped from the fusion zone and entered into the Al alloy. It could be ascribed to the stirring effect

Table 4 The atomic percent of the iron and aluminum in different Fe-Al IMC phases [1, 6, 28–31]

Zones	Fe-Al phases	Al (at.%)	Fe (at.%)	Hardness (HV) (10 g)
Fe-rich IMCs	Fe_3Al	12–28	66–80	250–350
	FeAl	Around 43	Around 53	400–520
Al-rich IMCs	$FeAl_2$	Around 51	Around 47	1000–1050
	Fe_2Al_5	51–74	26–37	1000–1100
	$FeAl_3$	Around 79	Around 19.5	820–980

Table 5 The atomic percent of the aluminum and copper in different Al-Cu IMC phases [26, 32–34]

Zones	Al-Cu phases	Al (at.%)	Cu (at.%)	Hardness (HV) (10 g)
Al-rich IMCs	Al_2Cu	68–74	25–31	630
Cu-rich IMCs	AlCu	Around 51	Around 49	905
	Al_3Cu_4	Around 48	Around 51	930
	Al_4Cu_9	15–30	70–84	770

resulting from strong convection in the welding pool under the action of keyhole [30, 39]. Finally, large amounts of isolated steel islands emerged with the high cooling velocity of molten pool.

The EDS results at the zone E_2 to H_2 in Fig. 5d are shown in Table 6. Based on Fe-Al [26] and Fe-Cu [33] binary phase diagram, the isolated steel island (zone E_2) could be identified as α-Fe (Al, Cu). According to Table 4 and the reported literatures [6, 26] in the laser welding of steel and aluminum alloy, the light gray phase (zone F_2) around the steel islands could be identified as Fe_2Al_5. According to Table 4, the needle-like phase could be considered as $FeAl_3$, which has been reported in the literatures [7, 26] about the laser welding of steel to aluminum alloy. Zone H_2 has almost the same element composition with zone D_2, so the dark gray phase could be identified as α-Al.

It is interesting that the Cu content at the upper margin of ligulate fusion zone is higher than that near the isolated steel islands in Table 6. Melted steel was mixed with melted Cu, and they both entered into the Al alloy during the initial period of welding. The Cu distributed along the interface of the Al/ fusion zone. Because melted Cu was limited, deeper penetration depth of steel wedging into aluminum alloy induced lower Cu content. Meanwhile, the degree of Cu mixture at the upper margins of ligulate fusion zone was lower than that at the bottom of the fusion zone. As a result, the Cu content at the upper margin of ligulate fusion zone is higher than that near the isolated steel islands. It can be seen that the effect improving metallurgical reaction of steel/Al alloy welding through Cu interlayer is weakened with increasing the deeper penetration depth of steel plunging into aluminum alloy.

3.2.2 Contact reaction brazing zone

The ligulate fusion zone has been discussed above, and the following discussion is primarily about the weld extension region with Cu-Al interfacial reaction layer. The weld extension region is shown in Fig. 6a, which is the magnified micrograph of zone B_1 in Fig. 3c. In the weld extension region, the Cu interlayer and the Al alloy matrix, to a certain extent, did not melt, and they were joined by contact reaction brazing mechanism.

Figure 6b, c shows the magnified micrograph of zone M_3 and N_3 in Fig. 6a, respectively. At the center of the contact reaction brazing zone, see Fig. 6b, the average thickness of the IMC layer was approximately 30 μm. The IMC layer consisted of typical columnar crystals with an average dimension of approximately 14×3.5 μm. There were small dendrites and network structures between the thick columnar crystals. And slender ribbon-shaped structure between IMC layer and Al matrix inlayed into aluminum alloy. At the edge of the weld extension region, see Fig. 6c, a distinct gap appeared between the Cu interlayer and IMC layer. The gap was considered to be a crack induced by thermal stress during welding. The IMC layer consisted of lump-like structure and network structure. The crystal morphology became smaller and more disordered compared with the columnar crystals in Fig. 6b.

Table 7 shows the EDS results at the zones A_3 to I_3 in Fig. 6b, c. The zone A_3 represents the copper matrix. According to Al-Cu binary phase diagram [37], the columnar crystal (zone B_3), small dendrite (zone C_3), and slender ribbon-shaped structure (zone F_3) in Fig. 6b could be all identified as Al_2Cu. Similarly, the lump-like structure (zones G_3 and H_3) in Fig. 6c could be identified as Al_2Cu. However, the light gray phase among the network structure (zone D_3 in Fig. 6b) or between the lump-like structures (zone I_3 in Fig. 6c) was identified as metastable phase of Al-Cu intermetallics. The supersaturated solid solution α-Al decomposed to form the metastable precipitates [40], such as θ′ and θ″, which are allomorphs of $A1_2Cu$. Because the high heating/cooling velocity during laser welding, there were little time to stay in the

Table 6 EDS analysis results of A_2 to H_2 in Fig. 5a, d (at.%) and phase distribution on different zones

Zones	A_2	B_2	C_2	D_2	E_2	F_2	G_2	H_2
Fe	90.25	24.42	2.36	1.64	80.23	22.12	10.78	1.78
Cu	3.22	19.84	15.64	0.84	3.19	1.07	1.62	0.88
Al	6.19	55.58	81.17	97.04	16.24	76.26	86.73	96.88
Cr + Mn	0.34	0.16	0.83	0.48	0.34	0.55	0.87	0.47
Phases	α-Fe	FeAl + $FeAl_2$ + Al-Cu intermetallics	α-Al + Al_2Cu	α-Al	α-Fe (Al, Cu)	Fe_2Al5	FeAl3	α-Al

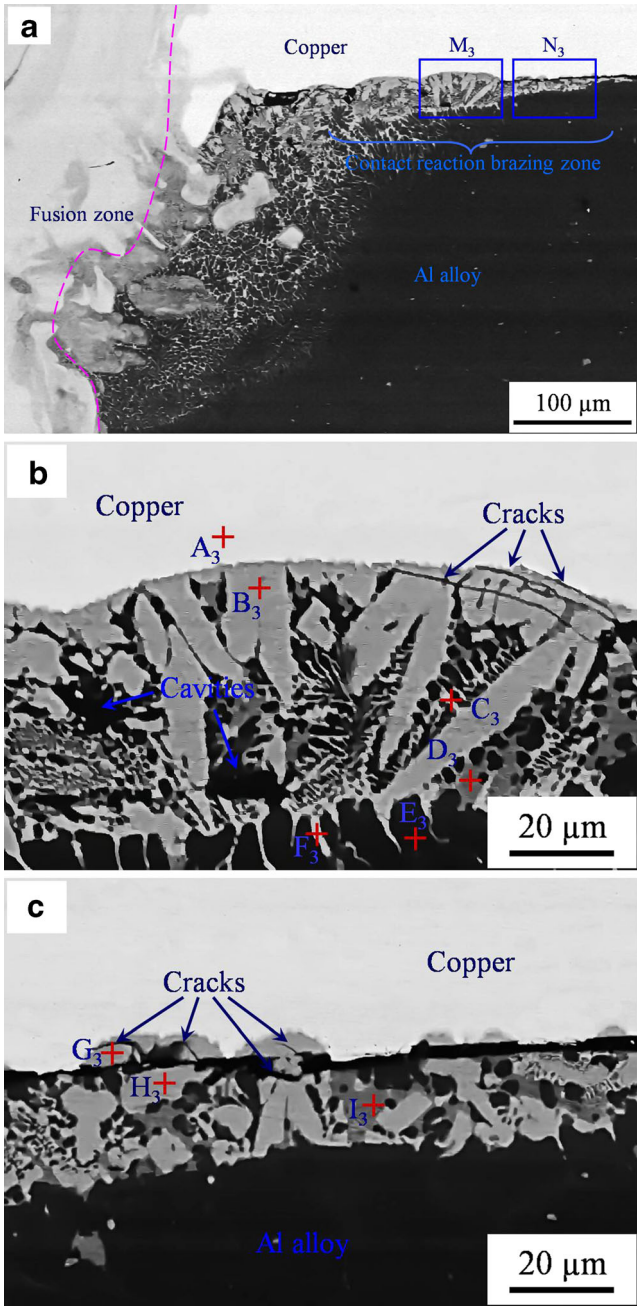

Fig. 6 Microstructures of contact reaction brazing zone: **a** from position B of Fig. 3c, **b** area M_3 in (**a**), and **c** area N_3 in (**a**)

range of aging temperature, which made the supersaturated α-Al not completely transform into $A1_2Cu$. The heavy gray phase (zone E_3) close to the parents of Al alloy could be identified as α-Al.

During the laser welding, contact reaction brazing occurred at weld extension region. Because the Cu-Al interface was far from the laser keyhole, the contact reaction brazing was induced by conductive heat from the molten pool. With increasing the interface temperature, the ability of atomic interdiffusion in the Cu-Al contact interface was enhanced. Once the interface composition was near the eutectic composition and the temperature was up to 548.2 °C (eutectic temperature), large quantity of liquid phase with low melting point would appear. The composition of the liquid phase was uneven, the Cu concentration near the Cu side was relatively high, and the Al concentration near the Al side was also relatively high. Because diffusion coefficient of atoms in the liquid phase was very large [41], the speed of the liquid phase composition homogenization was very fast. Meanwhile, atomic interdiffusion between the liquid phase and the Al matrix continued. The Cu atoms in the liquid phase diffused to Al matrix. When the Cu composition reached to eutectic composition, the Al matrix near the liquid phase dissolved, which made the thickness of the liquid phase increase. When the laser moved forward, the interface temperature decreased with the reduction of the conductive heat. Once the temperature was lower than the melting point of the liquid phase, crystallization began. But the thermal conductivity of Cu is almost triple of that of Al, see Table 2, the crystallization happened at the solid-liquid interface near the Cu interlayer. At last, eutectic products Al_2Cu was precipitated in the interfacial layer.

But shrinkage cavities (Fig. 6b) and micro-cracks (Fig. 6b, c) can be seen in the weld extension zone. Maybe there was no extra liquid phase to fill the spaces between the typical columnar crystals, which led to the formation of shrinkage cavities. Along the roots of columnar crystals, micro-cracks propagated between the Cu matrix and the gray phase Al_2Cu, which might be attributed to the stress concentration of the roots and the great differences of thermal expansion coefficient between Cu and Al_2Cu, as shown in Fig. 6b.

3.3 Mechanical property and fracture behavior

3.3.1 Mechanical property

Figure 7 shows tensile property of joints by a single/dual-beam laser. With the increasing of the welding speed, the tensile property of joints first increases and then decreases. A suitable range of welding speed is 0.9–1.25 m/min for dual-beam laser and 1.5–1.75 m/min for single-beam laser. It is consistent with the optimization range of welding speed obtained from weld appearance parameters. Obviously, the controllable range of optimum welding speed under dual-beam laser is wider than that under single-beam laser. Combined with the weld appearance of the joint, the most suitable welding speed is 1 m/min of dual-beam laser and 1.75 m/min of single-beam laser. Corresponding tensile properties of the joint are 65N/mm and 74N/mm, respectively.

According to the results reported by Y. Shi et al. [5], the shear strength of the joint made by single-beam laser welding was up to 71 MPa and the effective joining width was about 0.7 mm. Corresponding linear failure strength of joints was estimated to be 49.7 N/mm according to evaluation method of mechanical property in current investigation. In this paper, the

Table 7 EDS analysis results of A_3 to I_3 in Fig. 6b, c (at.%) and phase distribution on different zones

Zones	A_3	B_3	C_3	D_3	E_3	F_3	G_3	H_3	I_3
Fe	1.63	2.27	0.5	0	0	1.4	0	0	1.56
Cu	98.37	26.15	25.6	18.07	0.73	29.22	28.7	25.34	15.66
Al	0	71.59	73.9	81.93	99.27	69.39	71.3	74.66	82.78
Phases	Cu	Al_2Cu	Al_2Cu	Metastable phase of Al-Cu intermetallics	α-Al	Al_2Cu	Al_2Cu	Al_2Cu	Metastable phase of Al-Cu intermetallics

highest tensile property of the joint made by single-beam laser welding reached 64.8 N/mm. This benefited from the improving function of Cu interlayer on metallurgical reaction in the welding pool. First, the contact reaction brazing zone expanded effective joining width of the joint. Second, the Cu may have alloying function on Fe-Al intermetallics; similarly the Fe may have the same function on Cu-Al intermetallics.

When the welding speed was out of the suitable range, concavities and cracks appeared. These weld defects seriously deteriorated joint strength and even led to failure joining. However, at the suitable range of welding speed, weld defects were reduced. Moreover, a suitable welding speed could generate a suitable laser keyhole to form a controllable thickness of IMCs in interfacial reaction layer, which suppressed the liquid metal of molten pool to spatter in the Al alloy. As a result, the collapse was reduced and the load ability of the joint was enhanced.

Most important of all, the tensile property of dual beam, compared with single beam, is obviously enhanced as a whole. The maximum tensile property is improved from 64.8 N/mm (single beam) to 79.75 N/mm (dual beam). This phenomenon indicates that dual-beam laser enhances tensile property. The enhancement could be attributed to the increase of effective joining width and weld extension region width. From the view of linear energy, to obtain weld joints with good tensile property above 50 N/mm, a dual-beam laser needs to be 120–170 J/mm, which is wider than that of a single-beam laser about 50–60 J/mm.

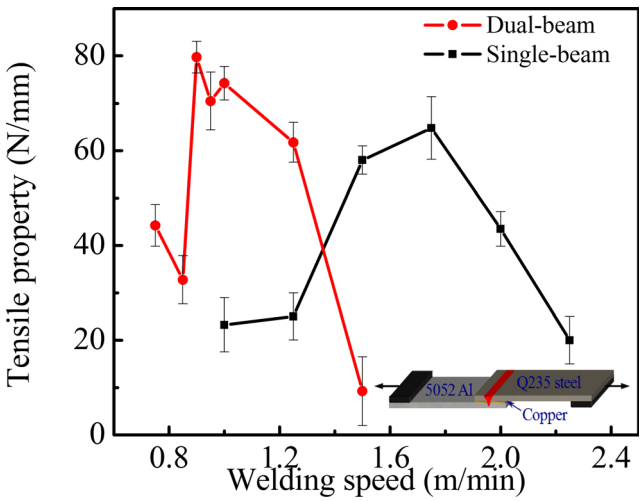

Fig. 7 Tensile property of joints welded by a single/dual-beam laser

Figure 8 shows the distribution of the microhardness at the penetration zone into Al alloy under a single/dual-beam laser. Obviously, there are two hardened zones in the cross section of single/dual beam, which are caused by the IMCs in interfacial reaction layer of Al alloy/fusion zone. The hardened zone of dual beam is wider than that of single beam. The reason is that the distance between the two beams' focused points, with regard to dual beam, is 0.8 mm. The hardness of single beam has lower values than that of dual beam. The reason is that the IMC layer of single beam was not thick enough to test, which was not like a dual beam having more disordered interface to produce large amounts of $FeAl_3$ phases.

The hardness of hardened zone can reach up to 697.9 HV, which is less than the average hardness (about 900 HV) of $FeAl_3$ phases (Table 4). Considering this situation, the addition of the copper-foil interlayer may improve the metallurgical reaction and promote the load-carrying ability of the joint. However, the new formed Al_2Cu may have detrimental effect on the mechanical property of the joint, which requires further study.

3.3.2 Fracture behavior

Figure 9a, c shows the fracture microstructures of the Cu interlayer side which were welded by a single/dual-beam laser,

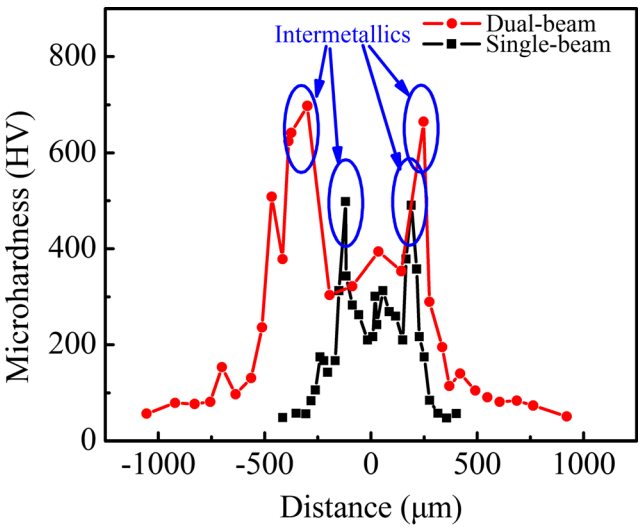

Fig. 8 Microhardness of joints welded by a single/dual-beam laser

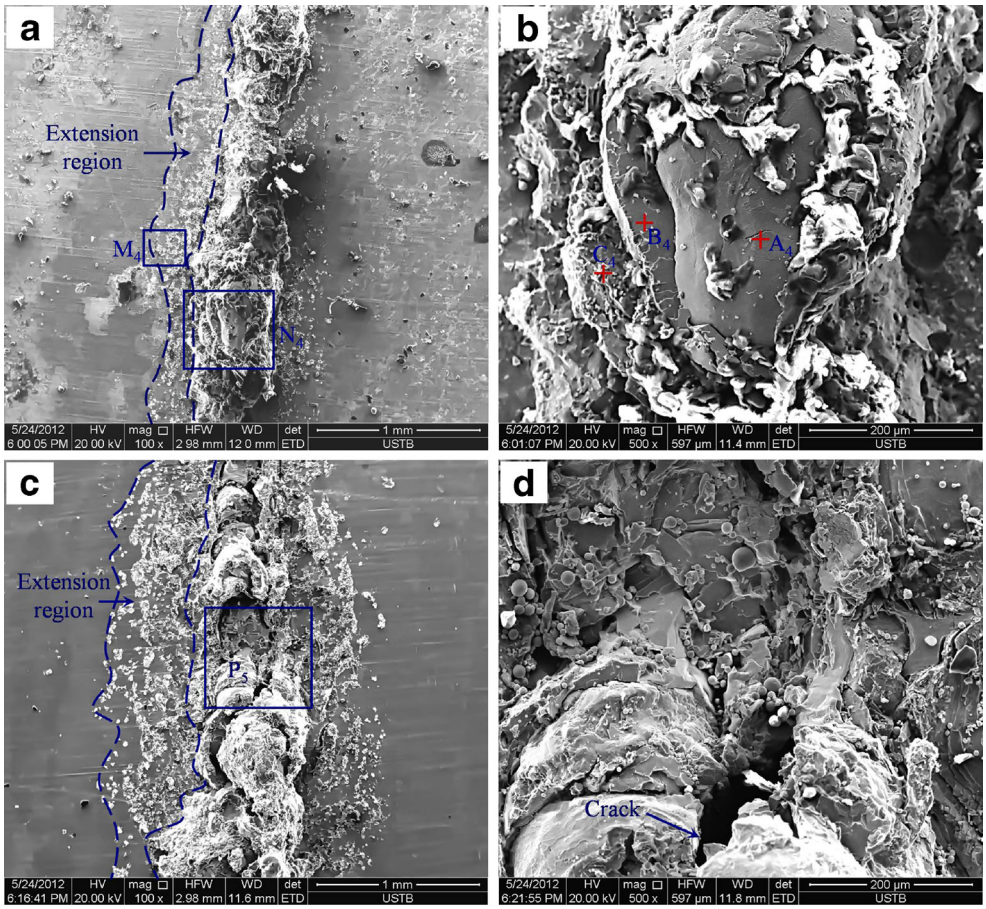

Fig. 9 Fracture microstructures on the side of steel: **a** obtained by a single-beam laser under the parameters of NO. 4 and **b** from zone N_4 in (**a**); **c** acquired by a dual-beam laser under the parameters of NO. 8 and **d** from zone P_4 in (**c**)

respectively. At the both sides of the weld seam metal, weld extension regions could be found close to the fusion zone. The width of weld extension region was nearly 280 μm in single-beam mode, but it was approximately 600 μm in dual-beam mode, which made the area of the contact reaction brazing increase. As a result, the effective joining width increased and the breaking strength of the weld joint was enhanced with a dual-beam laser.

Figure 9b, d shows the magnification of zone N_4 in Fig. 9a and zone P_4 in Fig. 9c, respectively. Table 8 shows the EDS analysis results of A_4 to C_4 in Fig. 9b. Considering the fact that zone A_4 is located at steel side (α-Fe), it was regarded as $FeAl_3$ attached to α-Fe, which could be proved by the appearance of $FeAl_3$ in the Fe-Al interface in Fig. 5d. According to Fe-Al binary phase diagram [26], the clear stratification facet (zone B_4) was identified as α-Fe (Al, Cu). The strong convection in the molten pool brought Al into the fusion zone and formed $FeAl_3$ IMC layer. Stress concentration at the brittle IMC layer under tensile stress led to fracture and formed the stratification facet. The phase composition of zone C_4 is very close to zone B_2 in Fig. 5a, which has been proved to mainly contain FeAl, $FeAl_2$, and a certain amount of Al-Cu intermetallics.

Table 8 EDS analysis results of A_4 to C_4 in Fig. 10b (at.%) and phase distribution on different zones

Zones	Fe	Cu	Al	Mg	Phases
A_5	61.06	5.45	33.49	0	α-Fe + $FeAl_3$
B_5	84.89	3.88	11.23	0	α-Fe (Al, Cu)
C_5	30.44	13.66	53.55	2.34	FeAl + $FeAl_2$ + Al-Cu intermetallics

As shown in Fig. 9b, d, the fracture surface has a relatively coarse transgranular cleavage facet, which is indicative of brittle rupture as the fracture mechanism. Previous studies [1, 42] have shown that $FeAl_3$ is the brittlest phase in aluminum-rich phases and has high microtwin density and low plasticity, which means the formation of $FeAl_3$ is accompanied by high stresses. Hence, the composite joints fractured can be positioned at the smooth surface of zone A_4, due to the $FeAl_3$ IMCs existing in zone A. Therefore, it can be concluded that $FeAl_3$ leads to the brittle fracture at the interfacial reaction layer. A clear crack along the weld seam, shown in Fig. 9d, indicates fracture may also occur in the fusion zone. The reason is that the strong convection brought Al into the fusion zone, which formed $FeAl_3$ IMCs and led to brittle fracture.

The fracture surface of contact reaction brazing zone in Cu side is shown in Fig. 10, which is the magnified micrograph of zone M_4 in Fig. 9a. At the edge of the contact reaction brazing

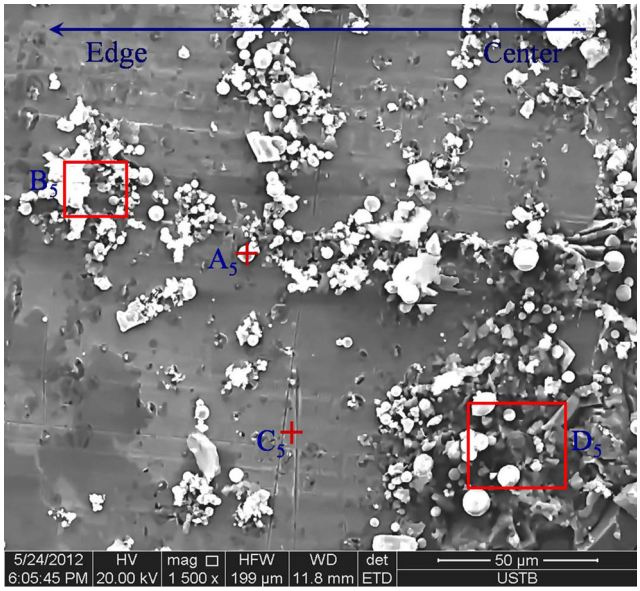

Fig. 10 Microstructure of fracture surface of the contact reaction brazing zone (magnification of zone M_4 in Fig. 9a)

zone, light spherical phases with different sizes aggregated and formed several light groups which distributed disorderedly. At the center, the light gray phases aggregated and formed a relatively large gray group. A certain amount of light spherical phases were attached to the gray group.

The EDS results of A_5 to D_5 in Fig. 10 are shown in Table 9. Based on Fe-Al [26] and Fe-Cu [33] binary phase diagram, the light spherical phase (zone A_5) attached to copper interlayer were identified as α-Fe (Al, Cu). It was sputtered from the weld region for the compelling convection of fusion steel. Zone B_5 contains the light group of spherical phases (α-Fe (Al, Cu)) and gray phases. Considering the fact that the high Cu content in zone B_5 was probably caused by the Cu plate, the gray phase in zone B_5 could be identified as Al_2Cu. Similarly, the gray phase (zone C_5), which is a very thin layer covered on the Cu plate, could be identified as Al_2Cu attached to the Cu plate. According to the Al-Cu binary phase diagram [37], the Al-Cu ratio in zone D_5 is around 2.5, which makes the relatively large gray group as a mix of eutectic phase Al_2Cu and α-Al phase.

As shown in Fig. 10, the light spherical phases and its groups appeared at the edge of the contact reaction brazing zone, where the contact reaction brazing was relatively weak. However, most contact reaction brazing zone at the center were almost completely covered by the thick eutectic structures of Al_2Cu and α-Al phase, due to the relatively strong contact reaction brazing between the copper interlayer and the Al matrix. It can be seen that the effect of contact reaction brazing is weakened with increasing distance away from the center of the contact reaction brazing zone.

Table 9 EDS analysis results of A_5 to D_5 in Fig. 10 (at.%) and phase distribution on different zones

Zones	Fe	Cu	Al	Mg	Phases
A_4	79.45	12.21	10.24	0	α-Fe (Al, Cu)
B_4	8.39	46.96	38.76	5.97	Al_2Cu
C_4	0	70.82	29.18	0	Cu + Al_2Cu
D_4	6.07	25.72	64.87	3.34	Al_2Cu + α-Al

4 Conclusions

The dissimilar metal lap-joint welding of Q235 low carbon steel and 5052 aluminum alloy with copper interlayer was investigated by a single/dual-beam laser. Based on the experiment results, the following main conclusions can be drawn:

1. The dual-beam laser welding, compared with single-beam laser welding, has better process stability, which makes better weld appearance, and bigger effective joining width which enhances tensile capacity. An ideal joint with fewer defects could be obtained when the welding speed is 0.9–1.25 m/min of dual-beam laser and 1.5–1.75 m/min of single-beam laser.
2. With a copper interlayer, a weld extension zone appeared between the copper interlayer and aluminum matrix through heat conduction from fusion zone, which enlarged effective joining zone. Combining with the microstructure characteristics and phase composition, the weld extension region was considered to be formed by the contact reaction brazing.
3. The microstructure of the welding joint by a single/dual-beam laser was composed of the ligulate fusion zone with Fe-Al interface and the contact reaction brazing zone with Al-Cu interface. The Fe-Al interface mainly consisted of α-Al and Al_2Cu eutectic structure, FeAl, $FeAl_2$, and a certain amount of Al-Cu intermetallics, Fe_2Al_5 and $FeAl_3$. The Al-Cu interface mainly consisted of eutectic phase Al_2Cu and metastable phase of Al-Cu intermetallics.
4. The fracture surface has transgranular cleavage facet, which is indicative of brittle rupture as the fracture mechanism. The $FeAl_3$ phases in the interfacial reaction layer may be still the main factor that leads to brittle rupture. The tensile property was enhanced by a dual-beam laser, and the addition of the copper-foil interlayer might improve the metallurgical reaction and promote the load-carrying ability of weld joint.

Acknowledgments The authors appreciate the financial support from the National Natural Science Foundation of China (No. 51475040) and Fundamental Research Funds for the Central Universities (FRF-TP-14-007A2).

References

1. Torkamany MJ, Tahamtan S, Sabbaghzadeh J (2010) Dissimilar welding of carbon steel to 5754 aluminum alloy by Nd:YAG pulsed laser. Mater Des 31:458–465
2. Sierra G, Wattrisse B, Bordreuil C (2008) Structural analysis of steel to aluminum welded overlap joint by digital image correlation. Exp Mech 48:21–23
3. Harooni M, Carlson B, Kovacevic R (2014) Dual-beam laser welding of AZ31B magnesium alloy in zero-gap joint configuration. Opt Laser Technol 56:247–255
4. Sierra G, Peyre P, Deschaux-Beaume F, Stuart D, Fras G (2007) Steel to aluminum key-hole laser welding. Mater Sci Eng A 447: 197–208
5. Shi Y, Zhang H, Takehiro W, Tang J (2010) CW/PW dual-beam YAG laser welding of steel/aluminum alloy sheets. Opt Laser Eng 48:732–736
6. Ma J, Harooni M, Clair B, Kovacevic R (2014) Dissimilar joining of galvanized high-strength steel to aluminum alloy in a zero-gap lap joint configuration by two-pass laser welding. Mater Des 58: 390–401
7. Chen SH, Huang JH, Ma K, Zhang H, Zhao XK (2012) Influence of a Ni-foil interlayer on Fe/Al dissimilar joint by laser penetration welding. Mater Lett 79:296–299
8. Brockmann R, Dickmann K, Radscheit C, Schubert E, Sepold G (1996) Method for the laser beam joining of aluminum and steel in the thin sheet range. Weld Cut 3:46–47
9. Mathieu A, Pontevicci S, Viala J, Cicala E, Matteï S, Grevey D (2006) Laser brazing of a steel/aluminum assembly with hot filler wire (88 % Al, 12 % Si). Mater Sci Eng A 435–436:19–28
10. Gao M, Chen C, Mei SW, Wang L, Zeng XY (2014) Parameter optimization and mechanism of laser–arc hybrid welding of dissimilar Al alloy and stainless steel. Int J Adv Manuf Technol 74:199–208
11. Qin GL, Su YH, Meng XM, Fu BL (2015) Numerical simulation on MIG arc brazing-fusion welding of aluminum alloy to galvanized steel plate. Int J Adv Manuf Technol. doi:10.1007/s00170-014-6529-5
12. Dharmendra C, Rao K, Wilden J, Reich S (2011) Study on laser welding-brazing of zinc coated steel to aluminum alloy with a zinc based filler. Mater Sci Eng A 528:1497–1503
13. Song J, Lin S, Yang C, Ma G, Liu H (2009) Spreading behavior and microstructure characteristics of dissimilar metals TIG welding-brazing of aluminum alloy to stainless steel. Mater Sci Eng A 509:31–40
14. Oikawa H, Ohimiya S, Yoshimura T, Saitoh T (1999) Resistance spot welding of steel and aluminum sheet using insert metal sheet. Sci Technol Weld Join 4(2):80–88
15. Choi C, Kim D, Nam D, Kim Y, Park Y (2010) A hybrid joining technology for aluminum/zinc coated steels in vehicles. J Mater Sci Technol 26(9):858–864
16. Pardal G, Meco S, Ganguly S, Williams S, Prangnell P (2014) Dissimilar metal laser spot joining of steel to aluminium in conduction mode. Int J Adv Manuf Technol 73:365–373
17. Liu X, Lan S, Ni J (2014) Analysis of process parameters effects on friction stir welding of dissimilar aluminum alloy to advanced high strength steel. Mater Des 59:50–62
18. Movahedi M, Kokabi AH, Seyed Reihani SM, Cheng WJ, Wang CJ (2013) Effect of annealing treatment on joint strength of aluminum/steel friction stir lap weld. Mater Des 44:487–492
19. Habibnia M, Shakeri M, Nourouzi S, Besharati Givi MK (2015) Microstructural and mechanical properties of friction stir welded 5050 Al alloy and 304 stainless steel plates. Int J Adv Manuf Technol 76:819–829
20. Sahin M (2009) Joining of stainless-steel and aluminium materials by friction welding. Int J Adv Manuf Technol 41:487–497
21. Tricarico L, Spina R, Sorgente D, Brandizzi M (2009) Effects of heat treatments on mechanical properties of Fe/Al explosion-welded structural transition joints. Mater Des 30:2693–2700
22. Tricarico L, Spina R (2010) Experimental investigation of laser beam welding of explosion-welded steel/aluminum structural transition joints. Mater Des 31:1981–1992
23. Çam G (2011) Friction stir welded structural materials: beyond Al-alloys. Int Mater Rev 56:1–48
24. Çam G, Erim S, Yeni Ç, Koçak M (1999) Determination of mechanical and fracture properties of laser beam welded steel joints. Weld J 78:193s–201s
25. Çam G, Yeni Ç, Erim S, Ventzke V, Koçak M (1998) Investigation into properties of laser welded similar and dissimilar steel joints. Sci Technol Weld Join 3:177–189
26. Meco S, Pardal G, Ganguly S, Miranda R, Quintino L, Williams S (2013) Overlap conduction laser welding of aluminium to steel. Int J Adv Manuf Technol 67:647–654
27. Miyashita Y, Borrisutthrkul R, Chen J, Mutoh Y (2007) Application of twin laser beam on AZ31/A5052 dissimilar metals welding. Key Eng Mater 353–358:1956–1959
28. Chen W, Molian P (2008) Dual-beam laser welding of ultra-thin AA 5052-H19 aluminum. Int J Adv Manuf Technol 39:889–897
29. Cicală E, Duffet G, Andrzejewski H, Grevey D, Ignat S (2005) Hot cracking in Al-Mg-Si alloy laser welding-operating parameters and their effects. Mater Sci Eng A 395:1–9
30. Qi X, Song G (2010) Interfacial structure of the joints between magnesium alloy and mild steel with nickel as interlayer by hybrid laser-TIG welding. Mater Des 31:605–609
31. Ren D, Liu L (2014) Interface microstructure and mechanical properties of arc spot welding Mg-steel dissimilar joint with Cu interlayer. Mater Des 59:369–376
32. Mai T, Spowage A (2004) Characterisation of dissimilar joints in laser welding of steel-kovar, copper-steel and copper-aluminum. Mater Sci Eng A 374:224–233
33. Yao C, Xu B, Zhang X, Huang J, Fu J, Wu Y (2009) Interface microstructure and mechanical properties of laser welding copper-steel dissimilar joint. Opt Laser Eng 47:807–814
34. Rathod B, Kutsuna M (2004) Joining of aluminum alloy 5052 and low-carbon steel by laser roll welding. Weld J 1:16s–26s
35. Lee K, Kumai S (2006) Characterization of intermetallic compound layer formed at the weld interface of the defocused laser welded low carbon steel/6111 aluminum alloy lap joint. Mater Trans 47(4): 1178–1185
36. Solchenbach T, Plapper P (2013) Mechanical characteristics of laser braze-welded aluminum-copper connections. Opt Laser Technol 54:249–256
37. Chen C, Hwang W (2007) Effect of annealing on the interfacial structure of aluminum-copper joints. Mater Trans 48(7):1939–1947
38. Zuo D, Hu S, Shen J, Xue Z (2014) Intermediate layer characterization and fracture behavior of laser-welded copper/aluminum metal joints. Mater Des 58:357–362
39. Fabbro R (2010) Melt pool and keyhole behaviour analysis for deep penetration laser welding. J Phys D Appl Phys 43(44):445–501
40. Ringer S, Hono K, Sakurai T (1995) Nucleation and growth of θ′ precipitation in Sn-modified A1-Cu alloys: APFIM/TEM observations. Appl Surf Sci 87/88:223–227
41. Wu M, Si N, Chen J (2011) Contact reactive brazing of Al alloy/Cu/stainless steel joints and dissolution behaviors of interlayer. Trans Nonferrous Metals Soc China 21:1035–1039
42. Agudo L, Eyidi D, Jank N, Bruckner J, Schmaranzer C, Arenholz E, Pyzalla AR (2007) Intermetallic Fe_xAl_y-phases in a steel/Al-alloy fusion weld. J Mater Sci 42:4205–4214